STRUCTURE, MAGNETIC AND OPTICAL
PROPERTIES OF MATERIALS

Investigation of the Structure and Properties of Magnetic Nanopowders of Magnetite−Maghemite Solid Solutions by SAPNS

O. A. Shilova[a, *], **A. S. Kovalenko**[a], **A. M. Nikolaev**[a],
T. V. Khamova[a], **I. Yu. Kruchinina**[a], **and G. P. Kopitsa**[a, b]

[a] *Grebenshchikov Institute of Silicate Chemistry, Russian Academy of Sciences, St. Petersburg, 199034 Russia*
[b] *Konstantinov Institute of Nuclear Physics, National Research Centre "Kurchatov Institute,"*
Gatchina, Leningradskaya oblast, 188300 Russia
***e-mail: olgashilova@bk.ru**

Abstract—Nanopowders of the magnetite−maghemite series have been synthesized by coprecipitation from aqueous solutions and by the sol−gel method, and a comparative comprehensive study of their structure has been carried out using X-ray diffraction analysis, scanning electron microscopy, low-temperature nitrogen adsorption, and small-angle polarized neutron scattering. It has been established that the resulting iron oxide nanopowders are porous systems that, depending on the synthesis method, have a one-level, two-level (for powders obtained by aqueous synthesis), or three-level (for powders obtained by the sol−gel method) hierarchical structure organization with different scales and different types of aggregation for each of the structural levels, and the characteristic size for the larger level in both cases is >45 nm. It has been revealed that the magnetic structure of the obtained iron oxide powders, regardless of the synthesis method, consists of superparamagnetic particles with a characteristic radius of magnetic $R_M \sim 4$ nm and magnetic−nuclear cross-correlations $R_{MN} \sim 3$ nm for powders obtained by the sol−gel method, and $R_M \sim 5{-}11$ nm and $R_{MN} \sim 4{-}8$ nm for powders obtained via aqueous route, depending on the synthesis conditions.

The method of fabricating magnetic nanoparticles by coprecipitation from aqueous salt solutions has long been widely used in practice [1−6]. Its advantages are associated primarily with the simplicity of the technological operations used, the availability of starting materials, and a small environmental impact [1]. The resulting nanoparticles do not need to be washed from organic solvents; they do not contain harmful toxic impurities. This is especially important when using powders in medicine and agriculture. The process can also be scaled up, for example, using microreactors with impinging swirling flows [7]. The main disadvantage of this method, as well as other liquid-phase methods for the synthesis of nanopowders, is a significant dependence of their structure and properties on the synthesis conditions at all stages of this process (selection and ratio of starting components, coprecipitation mode, extraction from the mother liquor, washing, drying, heat treatment). Despite the large number of studies on the production of magnetic nanopowders of magnetite and maghemite, there are no clear instructions in the scientific literature for reliable control over their shape, size, phase composition, superatomic structure, and magnetic properties. It

should be noted that during the synthesis by coprecipitation of iron(II, III) salts from aqueous solutions in air without the addition of oxidizing or reducing reagents, it is difficult to obtain nanopowders of magnetic nanoparticles with the composition corresponding to the pure phase of maghemite or magnetite. As our long-term studies have shown, under these conditions, the resulting nanoparticles, as a rule, have the phase composition of magnetite−maghemite solid solutions [8, 9].

Using classical research methods (X-ray powder diffraction analysis, scanning and transmission electron microscopy, IR spectroscopy, low-temperature nitrogen adsorption), it is almost impossible to quantitatively characterize the superatomic structure of nanopowders and the type of aggregation, which is crucial for their reproducible synthesis and practical use. At the same time, such an opportunity is provided by the small-angle X-ray scattering (SAXS) and small-angle neutron scattering (SANS) methods [10−14]. In particular, Danks et al. [15] note the breakthrough role of the SANS method for sol−gel synthesis and study of composites with specified morphological features.

Even greater difficulties arise when it is necessary to characterize the magnetic superatomic structure of nanopowders. To study the structure of nanosized powders, including iron oxides, scanning and transmission electron microscopy, X-ray diffraction analysis, and Mössbauer spectroscopy are usually used. However, these techniques do not provide information about the spatial distribution and nature of spin correlations in the material under study, although this is important for characterizing the structure. At the same time, this information can be obtained by using the SANS method, primarily the small-angle polarized neutron scattering (SAPNS) method [16−18], in particular, by determining the contribution of magnetic-nuclear interference in a nanopowder sample [19−24].

For magnetic nanopowders having the composition of magnetite−maghemite solid solutions with different ratios of Fe^{2+}/Fe^{3+} cations, we were able to find only a few similar studies [25−27] devoted to the study of their nuclear and magnetic mesostructure, including the assessment of the magnetic-nuclear component. At the same time, it is the structural features of the magnetic superatomic structure and its relationship with the phase composition and morphology of nanoparticles, their texture and magnetic properties that are of interest for the targeted use of nanoparticles, for example, in medicine and agricultural technologies [28−36].

This study focuses on quantitative characterization of the nuclear and magnetic superatomic structures of magnetite−maghemite nanopowders by the SAPNS method, correlation of these data with the characteristics obtained previously by classical methods, analysis of the influence of synthesis conditions (coprecipitation from aqueous solutions, sol−gel method) of nanopowders, and comparison of them with the characteristics of natural and commercial magnetite nanopowders.

To solve this problem, we relied on the data that we had previously obtained when studying the structure and properties of nanopowders of iron oxides of the maghemite−magnetite series synthesized by coprecipitation from aqueous solutions and the sol−gel method, as well as reference samples, commercial magnetite nanopowder and dispersed natural mineral magnetite [8, 13, 23, 31].

EXPERIMENTAL

Description of research objects. Magnetic iron oxide nanopowders were synthesized by two methods: coprecipitation from aqueous solutions and the sol−gel method. During the synthesis process, both by coprecipitation from aqueous solutions of iron(II, III) chlorides with aqueous ammonia, and by sol−gel route from a solution of iron(III) nitrate in ethylene glycol, various technological techniques were used to shift the synthesis process towards obtaining magnetic nanopowder of one of the phases, magnetite or maghemite (Table 1) [8, 9, 23, 30, 31]. During coprecipitation from aqueous solutions, the reaction mixture was subjected to ultrasonic homogenization or bubbling with argon on slight heating, the precipitate was modified with oleic acid or kept for a long time in the mother solution. In two cases, the synthesis of nanopowders by the sol−gel method was carried out under the same conditions, but heat treatment at high temperatures was carried out both in vacuum and in air.

A comprehensive study of the physicochemical properties of these nanopowders was carried out. Key characteristics of nanopowders are presented in Table 2.

X-ray powder diffraction analysis of the crystal lattice parameters of the oxides showed that all synthesized iron oxide nanopowders had a phase composition of the magnetite−maghemite series. The powders fabricated by coprecipitation from aqueous solutions had the composition of magnetite−maghemite solid solutions with different Fe^{2+}-to-Fe^{3+} ratios in them, while iron oxide nanopowders obtained by the sol−gel method had a composition closest to magnetite or maghemite.

A similar conclusion could be drawn from the IR spectroscopy data. The spectra revealed bands characteristic of both magnetite (580 cm^{-1}) and maghemite (559, 632 cm^{-1}) [35]. For a nanopowder with a surface modified by oleic acid, additional bands were found indicating its presence: 2927 (CH_2, asymmetric vibrations), 2852 (CH_2, symmetric vibrations), 1706 (C=O), and 1409 (CH_3) cm^{-1} [36].

A commercial powder and a pre-ground natural mineral powder were also studied for comparison and interpretation of data. Both powders corresponded to the phase composition of magnetite (Table 2).

Nanopowders obtained by a sol−gel route consisted of smaller nanoparticles (D_{CSD} ∼ 8−12 nm) compared to powders obtained by coprecipitation (D_{CSD} ∼ 12−19 nm) and to reference samples (D_{CSD} ∼ 61−63 nm).

Powders synthesized by both methods were magnetically soft materials, and their specific residual magnetization increased with an increase in particle size (Table 2).

All synthesized iron oxide nanopowders, regardless of the synthesis method, had a developed surface (S_{BET} ∼ 52−88 m^2/g) and a large specific mesopore volume ($V_{P/P_0 \to 0.99}$ = 0.26−0.43 cm^3/g) compared to commercial and natural magnetite powders (S_{BET} ∼ 12 and 2 m^2/g, $V_{P/P_0 \to 0.99}$ = 0.03 and 0.005 cm^3/g, respectively). At the same time, differences in synthesis methods have different effects on the pores shape and size, which indirectly indicates a difference in the superatomic structure, morphology, and type of aggregation of nanoparticles in the powders under study.

Table 1. Specific features of the different synthetic routes of magnetic nanopowders of iron oxides

Sample	Coprecipitation from aqueous solutions of $FeCl_2$ and $FeCl_3$ salts with aqueous ammonia			Composition
	stage: coprecipitation	stage: extraction for mother liquor, drying	powder color	
C/P 1	Ultrasonication 240 W, 40 kHz, 30 min [8, 9, 30, 31]	Magnetic separation, air drying, 100°C [8, 9, 30, 31]	Orange brown	γ-Fe_2O_3
C/P 2	Bubbling with argon, $T = 60°C$ [8, 9, 30, 31]	Magnetic separation, air drying, 100°C [8, 9, 30, 31]	Brown	Solid solution γ-Fe_2O_3−Fe_3O_4
C/P 3	Bubbling with argon, $T = 60°C$ plus: oleic acid, stirrer, 1 h [8, 9, 30, 31]	Decantation, air drying, 100°C [8, 9, 30, 31]	Brown	Solid solution γ-Fe_2O_3_Fe_3O_4@Oleic Acid
C/P 4	Magnetic stirrer, aging in the mother liquor for 16 h [8, 9, 30, 31]	Magnetic separation, air drying, 100°C [8, 9, 30, 31]	Dark brown	Solid solution Fe_3O_4−γ-Fe_2O_3
Sample	Sol−gel synthesis from a solution of $Fe(NO_3)_3·9H_2O$ in ethylene glycol $C_2H_4(OH)_2$			Composition
	stage: sol preparation	stage: sol−gel transition	stage: drying and heat treatment	powder color	
S/G 5	Magnetic stirrer, $T = 40°C$, 2 h [23]	$T = 80°C$, ~30 min [23]	Drying, $T = 120°C$, 4 h, vacuum heat treatment, $T = 300°C$, 2 h [23]	Black	Fe_3O_4
S/G 6	Magnetic stirrer, $T = 40°C$, 2 h [23]	$T = 80°C$, ~30 min [23]	Drying, $T = 120°C$, 4 h, air heat treatment, $T = 300°C$, 30 min [23]	Red brown	γ-Fe_2O_3 with an admixture of hematite

Reference samples were commercially available magnetite nanopowder (Sigma Aldrich, CAS no. 1317-61) and natural mineral magnetite from the Koikar deposit (Karelia, Russia) previously crushed to a nanometer level of dispersion.

Experimental techniques. SAPNS measurements were carried out on the KWS-1 small-angle diffractometer (FRM-II reactor, Garching, Germany) operating in a mode close to point geometry. The experiment used a beam of polarized neutrons with an initial polarization $P_0 \sim 0.95$ and a wavelength $\lambda = 0.5$ nm with $\Delta\lambda/\lambda = 0.1$. The sample−detector distance SD = 8 m made it possible to measure the neutron scattering intensity in the momentum transfer range $0.08 < q < 1$ nm^{-1}. Scattered neutrons were recorded with a two-dimensional scintillation position-sensitive detector based on ^{6}Li (128 × 128 cells with a spatial resolution of 5 × 5 mm^2).

The iron oxide powders were placed in a 1-mm thick quartz cell. The measurements were carried out in a "zero" field ($H \sim 0$) and an external magnetic field $H = 1$ T applied in the horizontal direction perpendicular to the incident neutron beam. In the experiment, we measured the dependence of the neutron scattering intensity on q for neutron polarization P_0 directed parallel to $I^+(q, P_0^+)$ and antiparallel $I^-(q, P_0^-)$ to the external magnetic field H. The initial spectra were corrected using a standard procedure, considering scattering by the installation fittings and quartz cell, as well as the laboratory hall background. To separate the isotropic and anisotropic scattering components, radial averaging of the intensity was carried out in the vicinity of the angles $\alpha = 0$ and $\pi/2$ in the detector plane (averaging sector $\pm 2°$), which corresponded to the directions along and across the applied magnetic field H. This averaging led to the system of equations:

$$\begin{cases} I^+(q,0) = I_{\parallel}^+(q) = \langle F_N^2(q) \rangle \\ I^+\left(q, \dfrac{\pi}{2}\right) = I_{\perp}^+(q) = \langle F_N^2(q) \rangle + \langle F_M^2(q) \rangle - 2P\langle F_N(q)F_M(q) \rangle \\ I^-(q,0) = I_{\parallel}^-(q) = \langle F_N^2(q) \rangle \\ I^-\left(q, \dfrac{\pi}{2}\right) = I_{\perp}^-(q) = \langle F_N^2(q) \rangle + \langle F_M^2(q) \rangle + 2P\varepsilon\langle F_N(q)F_M(q) \rangle \end{cases}. \tag{1}$$

Table 2. Characteristics of iron oxide nanopowders synthesized by coprecipitation from aqueous solutions of iron salts and by the sol–gel route in comparison with the commercial and natural magnetite and literature data

Sample (see Table 1)	Method of investigation					
	X-ray powder diffraction		SEM, TEM	low-temperature nitrogen adsorption		
	unit cell parameter a*, Å	CSD, nm	particle size/agglomerate size, nm	specific surface area S_{BET}, m²/g	specific pore volume $V_{P/P_0 \sim 0.995}$, cm³/g	pore shape and average diameter, nm
C/P 1	8.341(4)	14	~10−20/150	80.9 ± 1.4	0.29	Cylindrical, 13.4
C/P 2	8.355(4)	19	~15−20/50	51.7 ± 1.1	0.34	Slit-like, 24.2
C/P 3	8.359(4)	12	~5−10/50	75.0 ± 11.0	0.43	Slit-like, 1.9; 7.9
C/P 4	8.367(3)	13	~10−20/200	87.5 ± 1.6	0.26	Cylindrical, 11
S/G 5	8.402(3)	8	−/~100−400	63.5 ± 1.2	0.26	Bottle-shaped, 3.9
S/G 6	8.352(4)	12	−/~100−600	57.5 ± 0.6	0.26	Bottle-shaped, 6.3
Magnetite (natural mineral)	8.3840(3)	61	~100−500**	2.5 ± 0.5	0.005	Slit-like, 2.4
Magnetite commercial	8.3855(2)	63	~100/1000	12 ± 3	0.03	Slit-like, 2

 * According to literature data, the unit cell parameter (a) 8.336−8.339 Å for maghemite (γ-Fe$_2$O$_3$) [37, 38] and 8.396−8.397 Å for magnetite (Fe$_3$O$_4$) [37, 39].
** The particle size after dispersion of the natural mineral is given.

This system was used to determine the nuclear $\langle F_N^2(q)\rangle$, magnetic $\langle F_M^2(q)\rangle$, and interference $\langle F_N(q)F_M(q)\rangle$ contributions to the overall scattering intensity $I(q) = (I^+(q, P_0^+) + I^-(q, P_0^-))/2$.

Assuming that nuclear scattering is independent of magnetic field, the magnetic contribution to the scattering intensity at $H \sim 0$ was determined as:

$$\langle F_M^2(q)\rangle_{H\sim0} = \frac{3}{2}\left(I_{H\sim0}(q) - \langle F_N^2\rangle_{H=1\,T}\right). \quad (2)$$

The obtained scattering intensities were reduced to absolute values by normalizing to the incoherent scattering cross section of plexiglass, considering the detector efficiency and bulk density ρ_b for each powder. The QtiKWS software program was used for data preprocessing [40].

The magnetic properties of iron oxide powders were measured using an experimental setup based on the nuclear magnetic resonance (NMR) method, as described in detail in [41]. The magnetization was determined as the difference between the measured values of induction and strength of a constant and uniform magnetic field in accordance with the classical equation:

$$M = \frac{B}{\mu_0} - H, \quad (3)$$

where B is the magnetic field induction, μ_0 is the magnetic constant, and H is the magnetic field strength.

RESULTS AND DISCUSSION

Figure 1 shows two-dimensional scattering intensities on iron oxide samples obtained for two polarization states of the neutron beam ($I^-(q, \alpha)$ and $I^+(q, \alpha)$) during measurements in "zero" ($H \sim 0$) and horizontal magnetic fields ($H = 1$ T), respectively, as well as their difference $\Delta I_{MN}(q, \alpha) = I^-(q, \alpha) - I^+(q, \alpha)$ (magnetic-nuclear interference term) during measurements in an external magnetic field. For the spectra measured in a magnetic field $H = 1$ T, the observed scattering pattern is anisotropic with a significant change in the aspect ratios for the two polarization states (Fig. 1). The difference signal $\Delta I_{MN}(q, \alpha)$, where all background contributions are subtracted, shows an angular dependence on α with negligible intensity along the

direction of the applied magnetic field H. Separated contributions to scattering (nuclear $\left\langle F_N^2(q) \right\rangle$, magnetic $\left\langle F_M^2(q) \right\rangle_{H = 1\,T}$, and interference $\left\langle F_N(q)F_M(q) \right\rangle_{H = 1\,T}$) are presented in Figs. 2a−2e. From the above data, it is clear that nuclear scattering $\left\langle F_N^2(q) \right\rangle$ for all iron oxide nanopowders, with the exception of natural and commercial Fe_3O_4 samples, significantly (almost by an order of magnitude) exceeds magnetic scattering $\left\langle F_M^2(q) \right\rangle_{H = 1\,T}$.

SAPNS Nuclear Cross Section $d\Sigma_N(q)/d\Omega$ (H = 1 T)

The scattering pattern observed for the nuclear component of the scattering cross section $d\Sigma_N(q)/d\Omega$ SAPNS (Fig. 2) is characteristic of porous systems (solid phase−pore) with a disordered structure [10−14, 42−44]. At the same time, the behavior of $d\Sigma_N(q)/d\Omega$ depends on the conditions of synthesis of iron oxide nanopowders.

In particular, for nanopowders with a solid solution composition from the middle of the magnetite−maghemite series $\gamma\text{-}Fe_2O_3\text{−}Fe_3O_4$ (C/P 2, Fig. 2b), including nanopowders after surface modification with oleic acid $\gamma\text{-}Fe_2O_3\text{−}Fe_3O_4@OleicAcid$ (C/P 3) (Fig. 2c), the common feature is the presence of two q ranges on the scattering curves, where the behavior of $d\Sigma_N(q)/d\Omega$ obeys the power laws $q^{-\Delta}$ with different values of the exponents $\Delta = n_1$ and n_2, respectively. Near the crossover point q_c (the transition point from one scattering mode to the other), the behavior of $d\Sigma_N(q)/d\Omega$ is satisfactorily described by an exponential dependence (Guinier mode [45]). The observed SANS pattern is typical of scattering on two-level hierarchical structures with different characteristic scales and different types of aggregation for each level [14, 46, 47]. The convex shape of the $d\Sigma_N(q)/d\Omega$ ($n_1 > n_2$) curves clearly indicates that the inhomogeneities of the subsequent (larger in characteristic size R_c) structural level are formed from smaller inhomogeneities of the previous structural level, i.e. $R_{c2} > R_{c1}$.

It should be noted that the absence of deviation of the scattering curves $d\Sigma_N(q)/d\Omega$ from the power-law dependence q^{-n2} at small q values indicates that the characteristic size of second-level inhomogeneities R_{c2} exceeds the maximum size of inhomogeneities R_{max} scattering from which can be recorded in an experiment with the given resolution of the device. In this case, $R_{c2} > R_{max} \sim 3.5/q_{min} \sim 45$ nm [48].

Based on the above, to analyze the SANS data, we used a unified exponential-power expression that considers the presence of two structural levels in the scattering system [49]:

$$\frac{d\Sigma(q)}{d\Omega} = \sum_{i=0}^{1}\left(G_i\exp\left(-\frac{q^2 R_{gi}^2}{3}\right) + B_i\exp\left(-\frac{q^2 R_{g(i-1)}^2}{3}\right)\right) \times \left[\frac{\left(\text{erf}\left(\frac{qR_{gi}}{\sqrt{6}}\right)\right)^3}{q}\right]^{n_i}. \quad (4)$$

The summation is carried out over the number of structural levels. In general, this expression determines the presence of four free parameters for each structural level, such as the Guinier prefactor G_i, the gyration radius R_{gi}, the power prefactor B_i, and the exponent n_i.

In turn, for the nanopowder that is closest in composition to maghemite $\gamma\text{-}Fe_2O$ (C/P 1) (Fig. 2a) and, conversely, the one closest to magnetite, among the nanopowders obtained by coprecipitation of $Fe_3O_4\text{−}\gamma\text{-}Fe_2O_3$ (C/P 4) (Fig. 2d), two q ranges are also observed on the scattering curves, where the $d\Sigma_N(q)/d\Omega$ behavior is described by a power-law dependence $q^{-\Delta}$ with different exponents $\Delta = n_1$ and n_2. However, the closeness of the exponent n_2 to 1 indicates that the observed SANS occurs in systems consisting of randomly oriented, highly elongated anisodiametric (nonspherical) inhomogeneities of radius R_c and length L [50−52]. Therefore, their corresponding Guinier region should include two ranges of q. The absence of the second Guinier region in this case indicates that the length $L > R_{max} = 45$ nm. The range $q > q_c$, where the behavior of the scattering cross section $d\Sigma_N(q)/d\Omega$ is described by the power-law dependence q^{-n1}, corresponds to the Porod regime [53].

Thus, when analyzing the $d\Sigma_N(q)/d\Omega$ curves for $\gamma\text{-}Fe_2O_3$ (C/P 1) (Fig. 2a) and $Fe_3O_4\text{−}\gamma\text{-}Fe_2O_3$ (C/P 4) (Fig. 2d), a generalized empirical Guinier−Porod model was used [54]:

$$\begin{cases} \dfrac{d\Sigma(q)}{d\Omega} = \dfrac{G}{q^{n_2}}\exp\left(-\dfrac{q^2 R_g^2}{3 - n_2}\right) & \text{at } q < q_c \\ \dfrac{d\Sigma(q)}{d\Omega} = \dfrac{B}{q^{n_1}} & \text{at } q > q_c \end{cases}, \quad (5)$$

where $(3 - n_2)$ is the dimensional factor; G is the Guinier prefactor; R_g is the gyration radius, which is $R_g = R_c/\sqrt{2}$ for highly elongated objects; B is the power prefactor; n_1 is the exponent.

The behavior of the SANS cross section $d\Sigma_N(q)/d\Omega$ for natural Fe_3O_4 (Fig. 2e) is satisfactorily described by two power-law dependences:

$$\frac{d\Sigma(q)}{d\Omega} = \frac{B_2}{q^{n_2}} + \frac{B}{q^{n_1}} + I_{inc}, \quad (6)$$

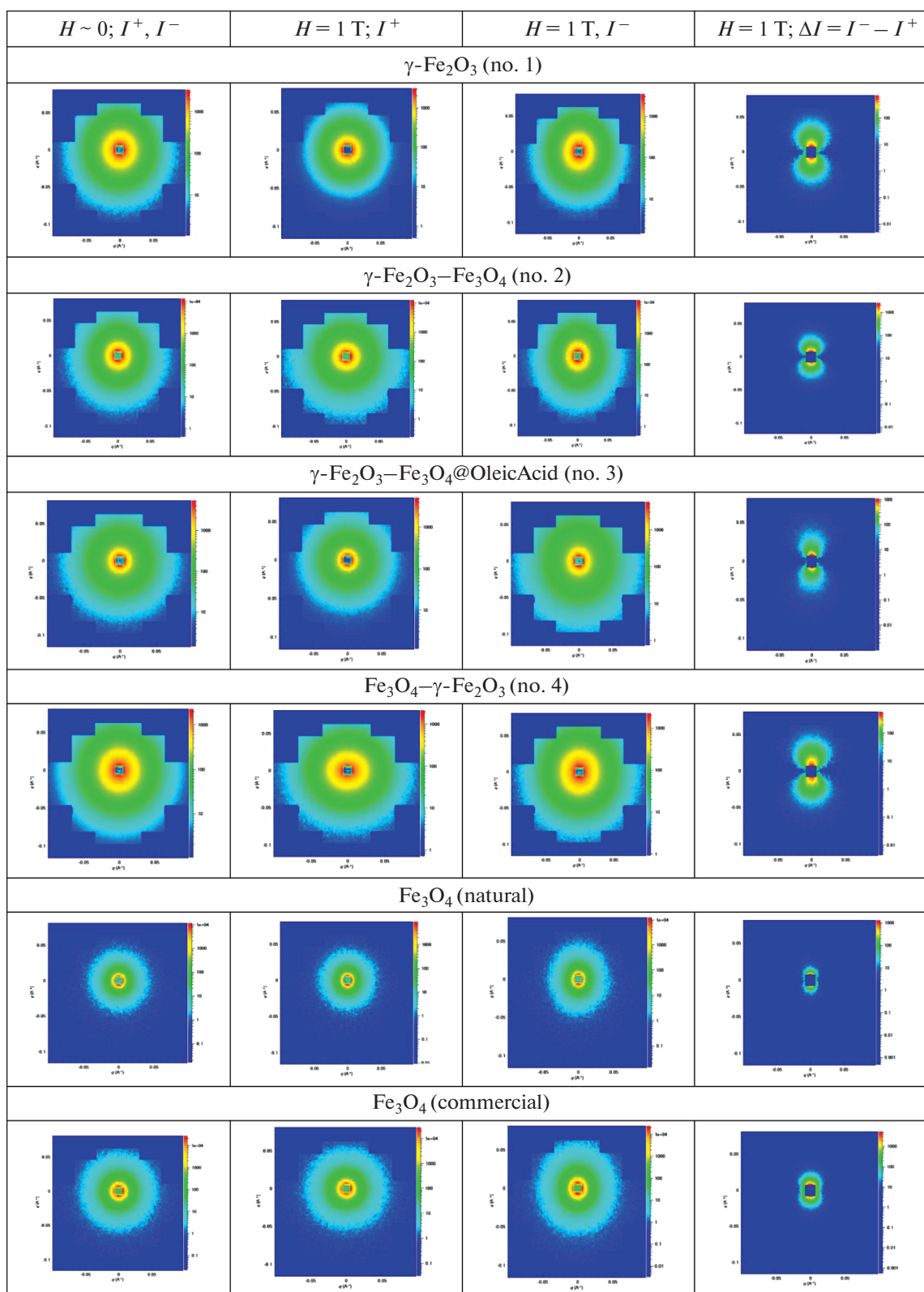which also corresponds to scattering on a disordered structure consisting of two types of inhomogeneities

$H \sim 0; I^{+}, I^{-}$	$H = 1$ T; I^{+}	$H = 1$ T, I^{-}	$H = 1$ T; $\Delta I = I^{-} - I^{+}$
γ-Fe$_2$O$_3$ (no. 1)			
γ-Fe$_2$O$_3$−Fe$_3$O$_4$ (no. 2)			
γ-Fe$_2$O$_3$−Fe$_3$O$_4$@OleicAcid (no. 3)			
Fe$_3$O$_4$−γ-Fe$_2$O$_3$ (no. 4)			
Fe$_3$O$_4$ (natural)			
Fe$_3$O$_4$ (commercial)			

Fig. 1. Experimental two-dimensional scattering intensities for two polarization states of the incident neutron beam and their difference $\Delta I_{\mathrm{MN}}(q, \alpha) = I^{-}(q, \alpha) - I^{+}(q, \alpha)$ obtained for iron oxide nanopowders during measurements in the external magnetic field $H = 1$ T. The square in the center of the detector is the trace from the beam absorber (beamstop).
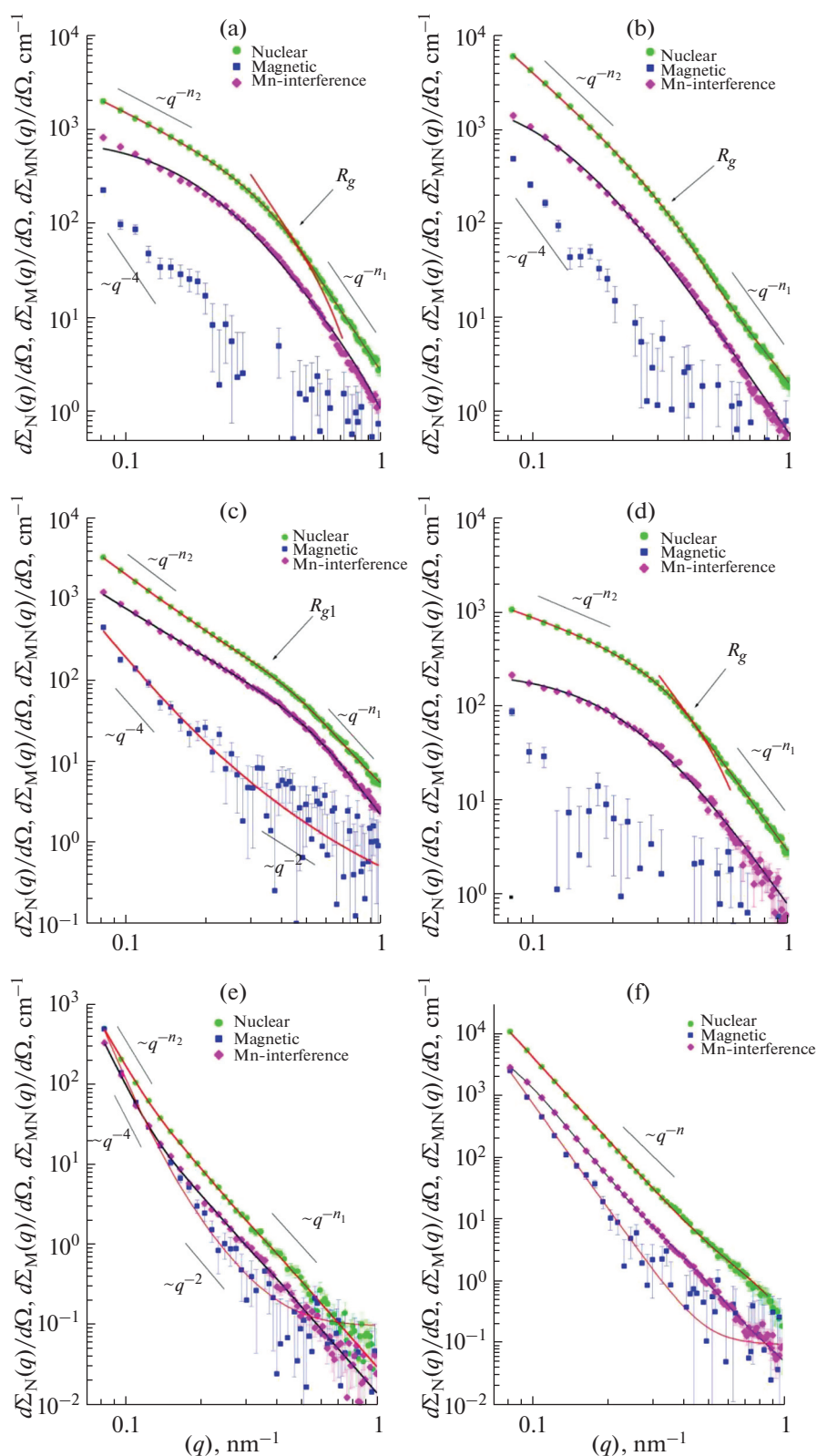
Fig. 2. Plots of nuclear $d\Sigma_N(q)/d\Omega$ ($\circ$), magnetic $d\Sigma_M(q)/d\Omega$ ($\square$), and magnetic-nuclear interference $d\Sigma_{NM}(q)/d\Omega$ ($\diamond$) contributions to the SAPNS cross sections vs. q obtained from the two-dimensional spectra (Fig. 1) for iron oxides (a) γ-Fe_2O_3 (no. 1), (b) γ-Fe_2O_3–Fe_3O_4 (no. 2), (c) γ-Fe_2O_3–Fe_3O_4@OleicAcid (no. 3), (d) Fe_3O_4–γ-Fe_2O_3 (no. 4), (e) natural Fe_3O_4, and (f) commercial Fe_3O_4. Solid lines show the results of experimental data fitting by Eqs. (4)–(7) and (9).

with different characteristic scales and different types of aggregation. At the same time, it is not possible to estimate the characteristic size R_{c1} of inhomogeneities of the first type from the available data due to the overlap in the corresponding q range of scattering from large-scale inhomogeneities of the second type, the characteristic size of which is $R_{c2} > R_{max} = 45$ nm.

For commercial Fe_3O_4, the observed SANS (Fig. 2f) in the entire q range is described only by a power-law dependence q^{-n}, which corresponds to scattering on magnetite particles with $R_c > R_{max} = 45$ nm.

The results obtained by convolution of Eqs. (4)–(6) with the installation resolution function and their least squares processing (LSM) are presented in Fig. 2 and Table 3.

According to the data obtained (Table 3), the γ-Fe_2O_3–Fe_3O_4 (C/P 2) nanopowder consists of almost smooth particles with a characteristic size $R_{c1} \sim 7$ nm, from which mass-fractal clusters with a dimension $D_M = 2.33$ are formed at the second structural level. At the same time, for the γ-Fe_2O_3–Fe_3O_4@OleicAcid (C/P 3) nanopowder modified with oleic acid, from particles of the first structural level with characteristic dimensions $R_{c1} \sim 6$ nm, having a developed fractal surface with a dimension $D_S = 2.55$, mass-fractal clusters with dimension $D_M = 2.41$ are formed at the second structural level. A similar picture of structure formation in the type of hierarchical fractal structures was previously observed for nanopowders of iron oxides Fe_3O_4 (S/G 5) and γ-Fe_2O_3 (S/G 6), synthesized by the sol–gel method [23].

In turn, nanopowders of composition, both practically corresponding to the composition of maghemite γ-Fe_2O_3 (C/P 1), and closer to magnetite Fe_3O_4–γ-Fe_2O_3 (C/P 4) (Table 3), consist of randomly oriented strongly elongated nonspherical (anisodiametric) particles with a gyration radius $R_c \sim 5$ and 6 nm, respectively. In the iron oxide γ-Fe_2O_3 nanopowder (C/P 1) these are practically smooth particles, while in the Fe_3O_4–γ-Fe_2O_3 (C/P 4) nanopowder, the particles have a developed fractal surface with the dimension $D_S = 2.30$. It should be noted that the characteristic particle sizes of the first structural level of all synthesized iron oxide nanopowders, obtained from the analysis of SANS data, generally correlate with the average crystallite sizes (D_{CSD}) obtained by XRD (Table 2).

Analysis of SANS data (Table 3) showed that commercial Fe_3O_4 powder consists of large-scale particles ($R_c > 45$ nm) having a diffuse interface surface ($n > 4$) [55], while natural Fe_3O_4 contains inhomogeneities of two types: large-scale inhomogeneities ($R_c > 45$ nm) with an almost smooth interface ($D_S \sim 2$) and smaller scale inhomogeneities with a developed fractal surface ($D_S = 2.46$).

SAPNS Magnetic Cross Section $d\Sigma_M(q)/d\Omega$ ($H = 1$ T)

For superparamagnetic nanoparticles upon magnetization saturation, magnetic scattering becomes completely anisotropic, while nuclear scattering remains isotropic. As can be seen from Fig. 2, the magnetic scattering cross section $d\Sigma_M(q)/d\Omega$ is statistically resolvable for natural and commercial Fe_3O_4, as well as for the γ-Fe_2O_3–Fe_3O_4@OleicAcid (C/P 3) solid solution. In this case, the behavior of magnetic scattering $d\Sigma_M(q)/d\Omega$ is satisfactorily described by power-law dependences:

$$\frac{d\Sigma(q)}{d\Omega} = \frac{B_2}{q^4} + \frac{B}{q^2} + I_{inc}, \qquad (7)$$

which corresponds to scattering on two types of spin correlations. The term q^{-4} corresponds to scattering on large-scale magnetic fluctuations, and q^{-2} is characteristic of scattering on spin correlations of the type of critical fluctuations [17].

For the remaining synthesized iron oxide nanopowders, the magnetic scattering cross section $d\Sigma_M(q)/d\Omega$ is small (no more than 10%) compared to nuclear scattering $d\Sigma_M(q)/d\Omega$ and is statistically resolvable only at small q values, $q < 0.15$ nm^{-1}, which corresponds to scattering on large-scale magnetic fluctuations that appear when saturation magnetization of the material is achieved. In this regard, a quantitative analysis of magnetic scattering $d\Sigma_M(q)/d\Omega$ for synthesized iron oxide samples is practically impossible. At the same time, this problem can be solved by analyzing the interference contribution $d\Sigma_{MN}(q)/d\Omega$ to the total SAPNS, which is determined by the product of the magnetic and nuclear scattering amplitudes, i.e. by the first, rather than the second, as in the case of intensity measurements, degree of magnetic scattering amplitude, which determines the higher sensitivity of the method [17].

SAPNS Magnetic–Nuclear Cross Section $d\Sigma_{MN}(q)/d\Omega$ ($H = 1$T)

Analysis of the magnetic–nuclear interference scattering contribution to the overall SAPNS in the $\alpha = \pi/2$ direction perpendicular to the applied magnetic field $H = 1$ T (Fig. 2) has demonstrated that the SAPNS $d\Sigma_{MN}(q)/d\Omega$ curves for nanopowders nearly corresponding to the maghemite γ-Fe_2O_3 composition (C/P 1) (Fig. 2a) and for solid solutions from the middle of the γ-Fe_2O_3–Fe_3O_4 series (C/P 2) (Fig. 2b), and shifted to magnetite Fe_3O_4–γ-Fe_2O_3 (C/P 4) (Fig. 2d) are satisfactorily fitted by the squared Lorentzian:

$$\frac{d\Sigma_{MN}(q)}{d\Omega}(q) = \frac{A}{\left(q^2 + \kappa^2\right)^2}, \qquad (8)$$

where A is a free parameter, and $\kappa = 1/R_{MN}$ is the inverse correlation radius of the magnetic-nuclear

Table 3. Superatomic structure parameters of synthesized iron oxide nanopowders and natural and commercial magnetite determined from analysis of the nuclear component SAPNS $d\Sigma_N(q)/d\Omega$

Parameters	C/P 1	C/P 2	C/P 3	C/P 4	Magnetite (natural mineral)	Magnetite commercial	S/G 5	S/G 6
R_{c3}, nm	–	–	–	–	–	–	>45	
n_3							3.18 ± 0.02	
$D_{M3} = n_3$			–	–				2.35 ± 0.02
$D_{S3} = 6 - n_3$				–			2.82 ± 0.02	–
R_{g2}, nm			>45				–	–
$R_{c2} = [(D_{S2,M2} + 2)/D_{S2,M2}]^{1/2} R_{g2}$, nm	–	–	–	–	–	–	5.1 ± 0.5	16 ± 3
n_2	0.95 ± 0.03	2.33 ± 0.02	2.41 ± 0.02	1.15 ± 0.03	–	4.00 ± 0.04	3.54 ± 0.06	2.74 ± 0.04
$D_{M2} = n_2$	–	2.33 ± 0.02	2.41 ± 0.02	–	–	–	–	2.74 ± 0.04
$D_{S2} = 6 - n_2$	–	–	–	–	–	4.00 ± 0.04	2.46 ± 0.06	–
$R_{c1} = \sqrt{(5/3)}\,R_{g1}$, nm	–	6.8 ± 1.3	5.7 ± 0.4	–	–	–	–	5.9 ± 0.8
$R_c = \sqrt{2}\,R_{g1}$, nm	4.7 ± 0.5			5.9 ± 0.7				
n_1	4.00 ± 0.05	3.97 ± 0.05	3.45 ± 0.05	3.70 ± 0.03	4.47 ± 0.02	3.54 ± 0.03	–	4.00 ± 0.05
$D_{S1} = 6 - n_1$	2.00 ± 0.05	2.03 ± 0.05	2.55 ± 0.05	2.30 ± 0.06	–	2.46 ± 0.06	–	–

R_{c1} is the characteristic radius of inhomogeneities of the first structural level, R_{c2} is the characteristic radius of inhomogeneities of the second structural level, R_{c3} is the characteristic radius of inhomogeneities of the third structural level, D_{S1} is the fractal dimension of inhomogeneities of the first structural level, D_{S2} is the fractal dimension of inhomogeneities of the second structural level, D_{S3} is the fractal dimension of inhomogeneities of the third structural level, D_{M2} is the fractal dimension of clusters of the second structural level, and D_{M3} is the fractal dimension of clusters of the third structural level.

Table 4. Characteristic sizes of iron oxide particles determined from analysis of XRD and SAPNS data as compared with remanent magnetization values

Sample	D_{CSD}, nm	R_c, nm	R_M, nm	R_{MN}, nm	M_{rem}, A/m	ρ_{bulk}, g/cm^3	$M_{sp. rem}$, A m^2/kg
C/P 1	14	4.7 ± 0.5	6.0 ± 0.7	4.7 ± 0.5	486.0	1.03	0.47
C/P 2	19	6.8 ± 1.3	11.2 ± 1.2	8.2 ± 0.7	1095.3	1.03	1.06
C/P 3	12	5.7 ± 0.4	4.7 ± 0.5	4.7 ± 0.5	250.0	0.97	0.26
C/P 4	13	5.9 ± 0.7	6.5 ± 0.7	4.1 ± 0.4	334.6	1.20	0.28
S/G 5	8.0	5.9 ± 0.8	–	2.7 ± 0.3	–	–	–
S/G 6	12	5.1 ± 0.5	4.1 ± 0.9	3.2 ± 0.4	–	–	–
Magnetite (natural mineral)	61	>45	>45	>45	–	–	–
Magnetite commercial	63	>45	>45	>45	2856.0	0.95	3.01

D_{CSD} is the coherent scattering domain size, R_c is the characteristic size of inhomogeneities, R_M is the characteristic size of magnetic fluctuations, R_{MN} is the characteristic size of magnetic-nuclear correlations, M_{rem} is the remanent magnetization, ρ_{bulk} is the bulk density, and $M_{sp. rem}$ is the specific remanent magnetization.

contrasting and, accordingly, scattering region. In coordinate representation, this expression corresponds to scattering on a spin correlator $\langle S_i, S_j \rangle$ that decays exponentially with distance r:

$$\langle S_i S_j \rangle \propto \exp\left(-\frac{r}{R_{MN}}\right). \tag{9}$$

In the case of a nanopowder fabricated by the same method as the C/P 2 nanopowder, but with the surface modified with oleic acid γ-Fe$_2$O$_3$–Fe$_3$O$_4$@Oleic Acid (C/P 3) (Fig. 2c), the observed magnetic-nuclear interference scattering is described by the sum of two terms:

$$\frac{d\Sigma_{MN}(q)}{d\Omega}(q) = \frac{A_2}{q^2} + \frac{A_1}{\left(q^2 + \kappa^2\right)^2}, \tag{10}$$

where the first term $\sim q^{-2}$ corresponds to the scattering on large-scale spin density fluctuations [17].

The results were obtained by convolution of Eqs. (7) and (9) with the setup resolution function and their processing using the LSM. The results obtained are presented in Fig. 2 and in Table 4.

According to Table 4, the characteristic sizes R_{MN} of magnetic-nuclear correlations obtained from the analysis of SAPNS are smaller than the characteristic sizes R_c of nuclear inhomogeneities (Table 3). However, the R_{MN} size correspond to the average sizes of magnetic-nuclear correlations, rather than to its upper limit, as in the case of the characteristic size R_c of nuclear correlations in the expressions used in the analysis of $d\Sigma_N(q)/d\Omega$.

SANS Magnetic Cross Section $d\Sigma_M(q)/d\Omega$ ($H \sim 0$ T)

Assuming that nuclear scattering is isotropic and independent of the applied magnetic field, we determined the magnetic contribution $\left\langle F_M^2(q) \right\rangle_{H\sim 0}$ to the

SANS intensity in the case of $H \sim 0$ by Eq. (2). The corresponding cross sections $d\Sigma_M(q)/d\Omega$ of the magnetic scattering for the synthesized iron oxide nanopowders are shown in Fig. 3. As can be seen, a statistically resolvable magnetic scattering $d\Sigma_M(q)/d\Omega$ is observed for all synthesized iron oxide nanopowders. In particular, for nanopowders γ-Fe$_2$O$_3$ (C/P 1) (Fig. 3a), γ-Fe$_2$O$_3$–Fe$_3$O$_4$ (C/P 2) (Fig. 3b), and Fe$_3$O$_4$–γ-Fe$_2$O$_3$ (C/P 4) (Fig. 3d), the SAPNS $d\Sigma_M(q)/d\Omega$ behavior, as in the case of the analysis of magnetic-nuclear interference for these samples (Figs. 2a, 2b, 2d), is satisfactorily described by a squared Lorentzian.

In the case of γ-Fe$_2$O$_3$–Fe$_3$O$_4$@OleicAcid (C/P 3) (Fig. 3c) nanopowder modified with oleic acid, an equation proportional to $\sim q^{-4}$ was used, which indicates the presence of large-scale spin density fluctuations in the scattering system.

The results presented in Fig. 3 and in Table 4 were obtained using the procedure described earlier.

Previously [23], we have comprehensively studied the supermolecular structure with an assessment of the nuclear and magnetic components for nanopowders synthesized by a sol–gel route. Features of the synthesis of these nanopowders and their properties, studied by classical methods, are given in Tables 1 and 2, and the parameters of the superatomic structure obtained from the analysis of the nuclear and magnetic-nuclear components are presented in Tables 3 and 4.

The comparative analysis by the SAPNS method of the nuclear superatomic structure of the synthesized iron oxide powders carried out in this work has demonstrated that they are porous systems, which, depending on the synthesis method, have a one-level (for C/P 1 and C/P 4 powders), two-level (for C/P 2 and C/P 3 powders), or three-level (for powders obtained by the sol–gel method) hierarchical structure organization with a different characteristic scale and type of aggregation for each of the structural lev-
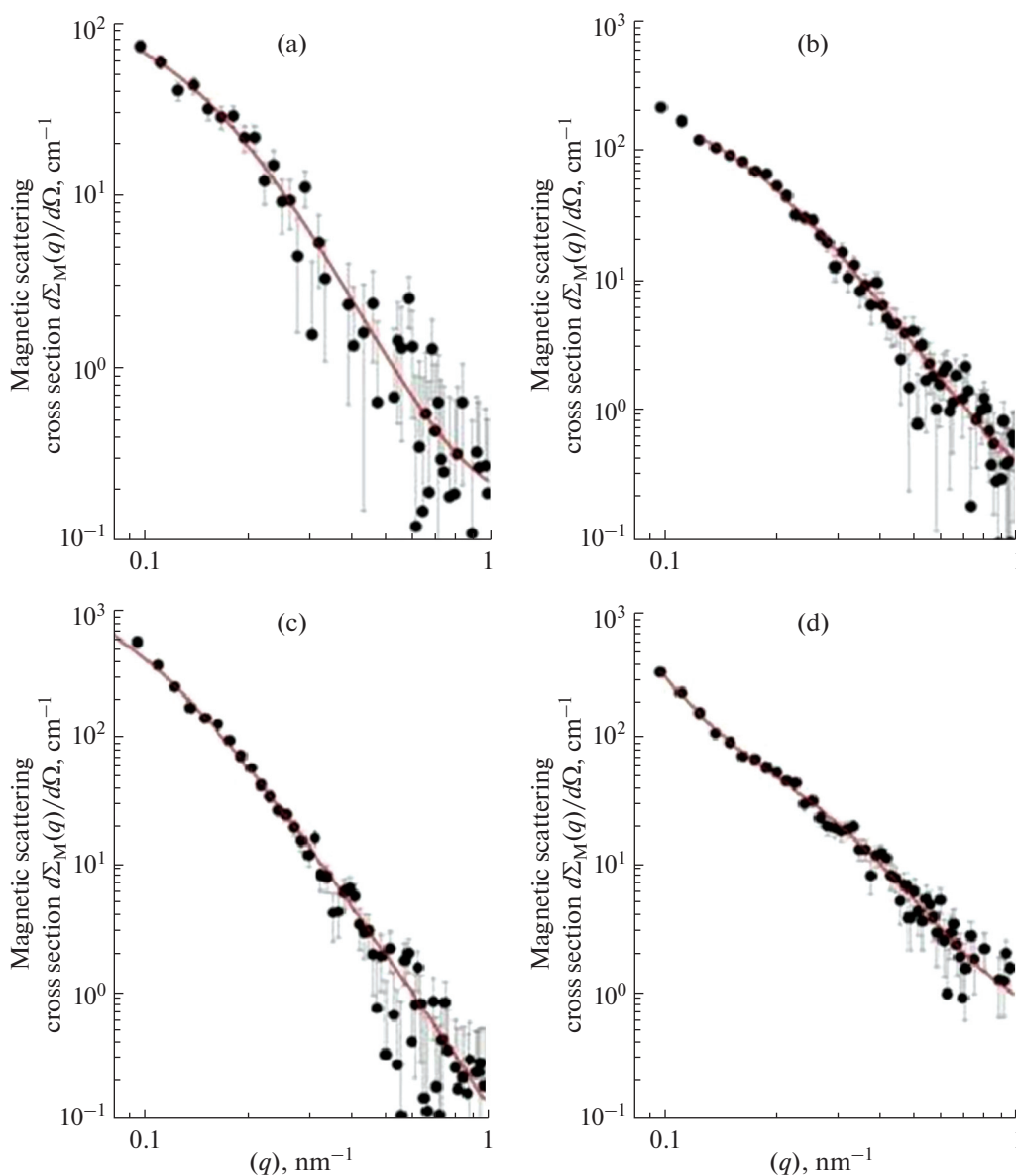
Fig. 3. SAPNS magnetic cross sections $d\Sigma_M(q)/d\Omega$ at $H \sim 0$ vs. q for iron oxides (a) γ-Fe$_2$O$_3$ (no. 1), (b) γ-Fe$_2$O$_3^-$Fe$_3$O$_4$ (no. 2), (c) γ-Fe$_2$O$_3$−Fe$_3$O$_4$@OleicAcid (no. 3), and (d) Fe$_3$O$_4$−γ-Fe$_2$O$_3$ (no. 4). Solid lines show the results of experimental data fitting by Eqs. (7) and (9).

els, and the characteristic size R_c for the larger level in both cases exceeds 45 nm.

In particular, powders prepared by coprecipitation from aqueous solutions, both practically corresponding to the composition of maghemite γ-Fe$_2$O$_3$ and those closer to magnetite Fe$_3$O$_4$−γ-Fe$_2$O$_3$, consist of randomly oriented, highly elongated nonspherical (anisodiametric) particles with a characteristic size $R_{c1} \sim 5$ and 6 nm, respectively. The γ-Fe$_2$O$_3$ powder consists of practically smooth particles, while in the powder closer in composition to magnetite Fe$_3$O$_4$−γ-Fe$_2$O$_3$, the particles have a developed fractal surface with the dimension $D_{S1} = 2.30$. The γ-Fe$_2$O$_3$−Fe$_3$O$_4$

solid solution powder consists of almost smooth particles with a characteristic size of $R_{c1} \sim 7$ nm, which form mass-fractal clusters with a dimension of $D_{M2} = 2.33$ at the second structural level. At the same time, for the γ-Fe$_2$O$_3$−Fe$_3$O$_4$ solid solution powder modified with oleic acid, particles of the first structural level with characteristic dimensions $R_{c1} \sim 6$ nm have a developed fractal surface with dimension $D_{S1} = 2.55$, which form mass-fractal clusters with dimension $D_{M2} = 2.41$ at the second structural level.

The first structural level of the γ-Fe$_2$O$_3$ powder obtained by the sol−gel method consists of almost smooth particles with a characteristic size of $R_{c1} \sim 6$ nm,

which at the second structural level aggregate into mass-fractal clusters with the dimension $D_{M2} = 2.74$ and the upper limit of self-similarity $R_{c2} \sim 16$ nm, which form mass-fractal aggregates with the dimension $D_{M3} = 2.35$ at the third structural level. At the same time, the Fe_3O_4 powder obtained by the sol−gel method at the first structural level also consists of small particles (according to SAXS data, $R_{c1} \sim 2$ nm) with an almost smooth surface, which at the second structural level aggregate into surface-fractal clusters with the dimension $D_{S2} = 2.46$ and the upper limit of self-similarity $R_{c2} \sim 5$ nm, forming surface-fractal aggregates with the dimension $D_{S3} = 2.82$ at the third structural level.

A detailed analysis of the SAPNS data made it possible to establish that the magnetic structure of the obtained iron oxide powders, regardless of the synthesis method, consists of superparamagnetic particles with a characteristic magnetic $R_M \sim 4$ nm and magnetic-nuclear cross-correlation radius $R_{MN} \sim 3$ nm for powders obtained by the sol−gel method, and $R_M \sim 5$−11 nm and $R_{MN} \sim 4$−8 nm for powders obtained by coprecipitation from aqueous synthesis, depending on the production conditions. In iron oxide powders synthesized by the sol−gel method, there are also spin correlations of the short-range order type between these superparamagnetic particles with interparticle magnetic correlation radii $\zeta_M \sim 16$ and 25 nm for Fe_3O_4 and γ-Fe_2O_3, respectively [23].

CONCLUSIONS

The structures of iron oxide powders synthesized by coprecipitation from aqueous solutions and by the sol−gel route have been comprehensively studied by XRD, SEM, low-temperature nitrogen adsorption, and small-angle polarized neutron scattering methods.

It has been established that the synthesized iron oxides are porous systems; depending on the synthesis method, they differ in the hierarchical organization of the structure with a characteristic scale and type of aggregation different for each of the structural levels. Powders obtained by coprecipitation from aqueous solutions are characterized by a one-level or two-level hierarchical organization of the structure, and powders obtained by the sol−gel method are characterized by a three-level structure. The characteristic size R_c for the larger level in both cases exceeds 45 nm. It has been found that the first structural level of γ-Fe_2O_3, Fe_3O_4 powders obtained by the sol−gel method, as well as powders that practically correspond to the composition of maghemite γ-Fe_2O_3 and the γ-Fe_2O_3−Fe_3O_4 solid solution obtained by coprecipitation, consists of almost smooth particles with a characteristic size $R_{c1} \sim$ 6, 2, 5, and 6 nm, respectively. At the same time, the first structural level of powders closer in composition to magnetite Fe_3O_4−γ-Fe_2O_3, and of the γ-Fe_2O_3−

Fe_3O_4 solid solution modified with oleic acid obtained by coprecipitation consists of particles with a developed fractal surface with the dimension $D_{S1} = 2.30$ and 2.55, respectively.

The second structural level was determined only for γ-Fe_2O_3, Fe_3O_4 powders obtained by the sol−gel method, as well as for γ-Fe_2O_3−Fe_3O_4 and γ-Fe_2O_3−Fe_3O_4 solid solution powders modified with oleic acid obtained by coprecipitation. It has been established that the primary particles of γ-Fe_2O_3 powders obtained by the sol−gel method, as well of the powders of the γ-Fe_2O_3−Fe_3O_4 solid solution and the γ-Fe_2O_3−Fe_3O_4 solid solution modified with oleic acid synthesized by coprecipitation, form at the second structural level mass-fractal clusters with dimensions $D_{M2} = 2.74$, 2.33, and 2.41, respectively, while primary particles of the Fe_3O_4 powder obtained by the sol−gel method form surface-fractal clusters with the dimension $D_{S2} = 2.46$.

The third structural level is observed only for γ-Fe_2O_3 and Fe_3O_4 powders obtained by the sol−gel method; at these level, mass-fractal aggregates with the dimension $D_{M3} = 2.35$ and surface-fractal aggregates with the dimension $D_{S3} = 2.82$, respectively, are formed.

Analysis of SAPNS data has demonstrated that the magnetic structure of the fabricated iron oxide powders, regardless of the synthesis method, consists of superparamagnetic particles with the characteristic magnetic $R_M \sim 4$ nm and magnetic-nuclear cross-correlation radius $R_{MN} \sim 3$ nm for powders obtained by the sol−gel method, and $R_M \sim 5$−11 nm and $R_{MN} \sim 4$−8 nm for powders obtained by coprecipitation from aqueous solutions, depending on the synthesis conditions.

CONFLICT OF INTEREST

The authors of this work declare that they have no conflicts of interest.

REFERENCES

1. M. I. Ferreira, T. Cova, J. A. Paixao, et al., *Woodhead Publishing Series in Electronic and Optical Materials. Magnetic Nanoparticle-Based Hybrid Materials* (Woodhead Publ, 2021).
   https://doi.org/10.1016/B978-0-12-823688-8.00033-8

2. M. Imran, A. H. Shaik, A. R. Ansari, et al., RSC Adv. **8**, 13970 (2018).
   https://doi.org/10.1039/C7RA13467C

3. H. Rashid, M. A. Mansoor, B. Haider, et al., Sep. Sci. Technol. **55**, 1207 (2020).
https://doi.org/10.1080/01496395.2019.1585876

4. J. C. Aphesteguy, G. V. Kurlyandskaya, J. P. Celis, et al., Mater. Chem. Phys. **161**, 243 (2015).
https://doi.org/10.1016/j.matchemphys.2015.05.044

5. M. Nazari, N. Ghasemi, H. Maddah, et al., J. Nanostruct. Chem. **4**, 99 (2014).
https://doi.org/10.1007/s40097-014-0099-9

6. J. A. Ramos Guivar, A. I. Martínez, A. O. Anaya, et al., Adv. Nanopart. **3**, 114 (2014).
https://doi.org/10.4236/anp.2014.33016

7. N. Yu. Fedorenko, R. Sh. Abiev, Yu. S. Kudryashova, et al., Ceram. Int. **48**, 13006 (2022).
https://doi.org/10.1016/j.ceramint.2022.01.174

8. O. A. Shilova, A. M. Nikolaev, A. S. Kovalenko, et al., Russ. J. Inorg. Chem. **65**, 426 (2020).
https://doi.org/10.1134/S0036023620030134

9. A. S. Kovalenko, O. A. Shilova, A. M. Nikolaev, et al., Colloid J. **85**, 389 (2023).
https://doi.org/10.1134/S1061933X23600239

10. S. Gopinath and J. Philip, Mater. Chem. Phys. **145**, 213 (2014).
https://doi.org/10.1016/j.matchemphys.2014.02.005

11. M. Zienkiewicz-Strzałka, M. Skibińska, and S. Pikus, Nucl. Instrum. Methods., Sect. B **411**, 72 (2017).
https://doi.org/10.1016/j.nimb.2017.03.028

12. H. Nirschl and X. Guo, Chem. Eng. Res. Des. **136**, 431 (2018).
https://doi.org/10.1016/j.cherd.2018.06.012

13. O. A. Shilova, A. M. Nikolaev, A. S. Kovalenko, et al., Ceram. Int. **47**, 28866 (2021).
https://doi.org/10.1016/j.ceramint.2021.07.047

14. T. V. Khamova, G. P. Kopitsa, A. M. Nikolaev, et al., Biointer. Res. Appl. Chem. **11**, 12285 (2021).
https://doi.org/10.33263/BRIAC114.1228512300

15. A. E. Danks, S. R. Hall, and Z. Schnepp, Mater. Horiz. **3**, 91 (2016).
https://doi.org/10.1039/c5mh00260e

16. A. I. Okorokov and V. V. Runov, Physica B **297**, 239 (2001).
https://doi.org/10.1016/S0921-4526(00)00843-7

17. M. R. Fitzsimmons and I. K. Schuller, J. Magn. Magn. Mater. **350**, 199 (2014).
https://doi.org/10.1016/j.jmmm.2013.09.028

18. S. Muhlbauer and D. Honecker, E. A. Périgo, et al., Rev. Mod. Phys. **91**, 015004 (2019).
https://doi.org/10.1103/RevModPhys.91.015004

19. D. Honecker, M. Bersweiler, S. Erokhin, et al., Nanoscale Adv. **4**, 1026 (2022).
https://doi.org/10.1039/D1NA00482D

20. S. H. Lee, D. H. Lee, H. Jung, et al., Curr. Appl. Phys. **15**, 915 (2015).
https://doi.org/10.1016/j.cap.2015.04.003

21. I. Bergenti, A. Deriu, L. Savini, et al., J. Magn. Magn. Mater. **262**, 60 (2003).
https://doi.org/10.1016/S0304-8853(03)00019-2

22. S. V. Grigoriev, S. V. Maleyev, A. I. Okorokov, et al., Europhys. Lett. **63**, 56 (2003).
https://doi.org/10.1209/epl/i2003-00477-3

23. T. V. Khamova, O. A. Shilova, Yu. E. Gorshkova, et al., Nanosystems: Phys. Chem. Math. **13**, 414 (2022).
https://doi.org/10.17586/2220-8054-2022-13-4-414-429

24. V. V. Runov, A. N. Bugrov, R. Yu. Smyslov, et al., Russ. J. Inorg. Chem. **66**, 225 (2021).
https://doi.org/10.1134/S0036023621020170

25. Z. Fu, Y. Xiao, A. Feoktystov, et al., Nanoscale **8**, 18541 (2016).
https://doi.org/10.1039/c6nr06275j

26. D. Zákutná, D. Nižňanský, L. C. Barnsley, et al., Phys. Rev. X **10**, 031019 (2020).
https://doi.org/10.1103/PhysRevX.10.031019

27. T. Köhler, A. Feoktystov, O. Petracic, et al., Nanoscale **13**, 6965 (2021).
https://doi.org/10.1039/d0nr08615k

28. R. S. Chouhan, M. Horvat, J. Ahmed, et al., Cancers **13**, 2213 (2021).
https://doi.org/10.3390/cancers13092213

29. H.-V. Tran, N. M. Ngo, R. Medhi, et al., Materials **15**, 503 (2022).
https://doi.org/10.3390/ma15020503

30. A. S. Kovalenko, A. M. Nikolaev, T. V. Khamova, et al., Glass Phys. Chem. **47**, 67 (2021).
https://doi.org/10.1134/S1087659621070063

31. O. A. Shilova, G. G. Panova, A. M. Nikolaev, et al., Lett. Appl. NanoBioScience **10**, 2215 (2021).
https://doi.org/10.33263/LIANBS102.22152239

32. Y. Wang, S. Wang, M. Xu, et al., Environ. Pollut. **249**, 1011 (2019).
https://doi.org/10.1016/j.envpol.2019.03.119

33. M. Serpoush, M. Kiyasatfar, and J. Ojaghi, Mater. Today: Proc. **65** Part 6, 2915 (2022).
https://doi.org/10.1016/j.matpr.2022.06.441

34. Ch. Turrina, A. Klassen, D. Milani, et al., Heliyon **9**, e16487 (2023).
https://doi.org/10.1016/j.heliyon.2023.e16487

35. P. R. S. Baabu, H. K. Kumar, M. B. Gumpu, et al., Materials **16**, 59 (2023).
https://doi.org/10.3390/ma16010059

36. J. Ibarra, J. Melendres, M. Almada, et al., Mater. Res. Exp. **2**, 095010 (2015).
https://doi.org/10.1088/2053-1591/2/9/095010

37. S. Nasrazadani and A. Raman, Corros. Sci. **34**, 1355 (1993).
https://doi.org/10.1016/0010-938X(93)90092-U

38. C. Pecharroman, T. Gonzalez-Carreno, and J. E. Iglesias, Phys. Chem. Miner. **22**, 21 (1995).
https://doi.org/10.1007/BF00202677

39. J. W. Anthony, R. A. Bideaux, and K. W. Bladh, *Magnetite. Handbook of Mineralogy* (Mineralogical Society of America, Chantilly VA, 2018).

40. Jülich Centre for Neutron Science, QtiKWS 2019. Available online: www.qtisas.com.

41. A. I. Zhernovoi and S. V. D'yachenko, Techn. Phys. **60**, 595 (2015).
https://doi.org/10.1134/S1063784215040325

42. D. W. Schaefer and R. S. Justice, Macromolecules **40**, 8501 (2007).
https://doi.org/10.1021/ma070356w

43. A. E. Baranchikov, G. P. Kopitsa, K. E. Yorov, et al., Russ. J. Inorg. Chem. **66**, 874 (2021).
https://doi.org/10.1134/S003602362106005X

44. S. Koizumi, Z. Yue, Y. Tomita, et al., Eur. Phys. J. E **26**, 137 (2008).
https://doi.org/10.1140/epje/i2007-10259-3

45. A. Guinier, G. Fournet, C. B. Walker, and K. L. Yudowitch, *Small-Angle Scattering of X-rays* (Wiley, New York, 1955).

46. G. Beaucage, T. A. Ulibarri, E. P. Black, et al., *Hybrid Organic-Inorganic Composites*, Eds. By Mark J. et al., (ACS Symposium Series, American Chemical Society, Washington DC, 1995).

47. M. Štěpánek, P. Matějíček, K. Procházka, et al., Langmuir **27**, 5275 (2011).
https://doi.org/10.1021/la200442s

48. H. D. Bale and P. W. Schmidt, Phys. Rev. Lett. **53**, 596 (1984).
https://doi.org/10.1103/PhysRevLett.53.596

49. G. Beaucage, J. Appl. Crystallogr. **28**, 717 (1995).
https://doi.org/10.1107/S0021889895005292

50. L. A. Ivanova, K. B. Ustinovich, T. V. Khamova, et al., Materials **13**, 2087 (2020).
https://doi.org/10.3390/ma13092087

51. P. T. Larsson, J. Stevanic-Srndovic, S. V. Roth, et al., Cellulose **29**, 117 (2022).
https://doi.org/10.1007/s10570-021-04291-x

52. J. D. Guild, S. T. Knox, S. B. Burholt, et al., Macromolecules **56**, 6426 (2023).
https://doi.org/10.1021/acs.macromol.3c00585

53. G. Porod, Kolloid-Zeitschrift **125**, 51 (1952).
https://doi.org/10.1007/BF01519615

54. B. Hammouda, J. Appl. Crystallogr. **43**, 716 (2010).
https://doi.org/10.1107/S0021889810015773

55. P. W. Schmidt, D. Avnir, D. Levy, et al., J. Chem. Phys. **94**, 1474 (1991).
https://doi.org/10.1063/1.460006

Translated by G. Kirakosyan